Effect of Percolation on the Capacitance of Supercapacitor Electrodes Prepared from Composites of Manganese Dioxide Nanoplatelets and Carbon Nanotubes

Thomas M. Higgins,[†,‡] David McAteer,[†,‡] João Carlos Mesquita Coelho,[†,§] Beatriz Mendoza Sanchez,[†,§] Zahra Gholamvand,[†,‡] Greg Moriarty,[†,‡] Niall McEvoy,[†,§] Nina Christina Berner,[†,§] Georg Stefan Duesberg,[†,§] Valeria Nicolosi,[†,‡,§] and Jonathan N. Coleman*[,†,‡]

[†]CRANN and AMBER Research Centres, Trinity College Dublin, Dublin 2, Ireland, [‡]School of Physics, Trinity College Dublin, Dublin 2, Ireland, and [§]School of Chemistry, Trinity College Dublin, Dublin 2, Ireland

ABSTRACT Here we demonstrate significant improvements in the performance of supercapacitor electrodes based on 2D MnO_2 nanoplatelets by the addition of carbon nanotubes. Electrodes based on MnO_2 nanoplatelets do not display high areal capacitance because the electrical properties of such films are poor, limiting the transport of charge between redox sites and the external circuit. In addition, the mechanical strength is low, limiting the achievable electrode thickness, even in the presence of binders. By adding carbon nanotubes to the MnO_2-based electrodes, we have increased the conductivity by up to 8 orders of magnitude, in line with percolation theory. The nanotube network facilitates charge transport, resulting in large increases in capacitance, especially at high rates, around 1 V/s. The increase in MnO_2 specific capacitance scaled with nanotube content in a manner fully consistent with percolation theory. Importantly, the mechanical robustness was significantly enhanced, allowing the fabrication of electrodes that were 10 times thicker than could be achieved in MnO_2-only films. This resulted in composite films with areal capacitances up to 40 times higher than could be achieved with MnO_2-only electrodes.

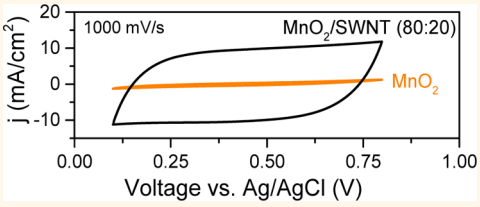

KEYWORDS: supercapacitor · percolation · capacitance · nanotube · manganese dioxide · carbon nanotube composite · electrode · thin film · nanosheet · two-dimensional

Over the past decade, the study of two-dimensional (2D) nanomaterials has become one of the most exciting areas of nanoscience. Catalyzed by the exciting properties of graphene,[1] a large research field has grown up around the study of 2D materials such as MoS_2,[2,3] MnO_2[4] and most recently phosphorene.[5] These materials can either be grown over large areas[2] or produced in large quantities by exfoliation of layered compounds.[6−9] A host of 2D nanostructures have shown great promise for applications in a range of areas from optoelectronics[3] to electrochemistry.[2,10,11] Possibly the most exciting area where 2D materials have shown potential is in the generation and storage of energy. The versatility of these materials is clearly illustrated by the range of energy applications where they have been applied: transition metal dichalcogenides such as MoS_2 and WS_2 have been demonstrated as hydrogen evolution catalysts,[2,12,13] electrodes in lithium ion batteries[2,14,15] and dye-sensitized solar cell electrodes;[16] layered oxides such as TiO_2 and MnO_2 as lithium ion battery electrodes[17−19] or oxygen reduction catalysts;[20] while 2D materials such as Bi_2Te_3 have been demonstrated as efficient thermoelectrics.[21]

However, one of the most promising applications of 2D materials is as electrodes in supercapacitors. Many of these compounds display redox properties resulting in levels of Faradaic- or pseudocapacitances much higher than those achievable from electrochemical double layer effects alone.[22−24] Indeed, the theoretical pseudocapacitance of

* Address correspondence to colemaj@tcd.ie.

Received for review July 15, 2014 and accepted September 8, 2014.

Published online September 08, 2014
10.1021/nn5038543

MnO_2 is 1370 F/g, which is extremely high.[25] Moreover, a growing selection of layered oxides and hydroxides are showing great promise in this area.[3,26−35]

To best employ the high intrinsic pseudocapacitance of any material requires the maximum number of redox active sites be in contact with the electrolyte and therefore available for charge storage. This makes the layered oxides described above extremely attractive so long as they can be exfoliated into thin flakes. Indeed, electrodes fabricated from monolayers of MnO_2 or RuO_2 would be expected to display very high capacitances as all redox sites would be adjacent to the electrolyte. Probably the best way to achieve this in practice is to employ liquid exfoliation of layered compounds to give large quantities of suspended flakes in a processable form.[4,7] Even though the flakes produced by such techniques may not be exclusively monolayers, but display a range of thicknesses up to 10 layers thick, the scalability[36] of such exfoliation processes coupled with the intrinsic processability[7] of liquid suspensions makes liquid exfoliation an attractive way to produce supercapacitor electrodes.

However, whether for supercapacitors produced by liquid processing or other means, experimental pseudocapacitances approaching the theoretical values are seldom achieved except for ultrathin electrodes which are charged and discharged very slowly.[25,37,38] It has not proven straightforward to transform such promise into practical supercapacitors with high absolute capacitance. One of the reasons for this is that the specific capacitance (*i.e.*, in F/g) generally falls rapidly with electrode thickness. This was noted by Lee *et al.*, reporting a specific capacitance of only 0.13 F/g for a 20 μm thick MnO_2 film (2 mV/s).[39] Such unfavorable thickness-dependence is a general problem for low-conductivity electrode materials and is associated with limitations in the transport of both electrons and ions.[40,41] These problems are serious as they also mean that the available capacitance falls dramatically at high charge/discharge rates. In addition, the low electrical conductivity results in high equivalent series resistances and consequently low power densities.

One common solution to this problem is to combine the pseudocapacitive material with a nanoconductor such as carbon-black, acetylene black, carbon nanotubes or graphene to form a composite electrode.[30,39,42−46] It is worth noting that such an approach is straightforward when using solution processing techniques.[6,47] Numerous researchers have shown that this strategy can result in increased capacitance by facilitating transport of charge from redox sites to the external circuit.[33,39,42,48,49] However, there are a number of problems with this approach. Most important is that any addition of nanoconductor reduces the fraction of capacitive material present. Thus, it is critical to fully characterize such composites to identify the minimum nanoconductor mass fraction required. This requires the preparation of a large number of composite electrodes over a wide range of mass fractions and their characterization *via* complementary electrical and capacitive measurements. Particular care must be taken with novel composites where both phases are nanomaterials which may have different dimensionalities (*e.g.*, 1D nanotubes and 2D nanosheets or nanoplatelets). The electrical properties,[47] and so the optimum nanoconductor content, will vary strongly across composite types. This means extensive optimization is required in every case, which is not generally done. These problems are especially relevant for composites containing 2D nanomaterials, in particular, those involving new materials are not yet well documented. Indeed, we suggest that for most composite supercapacitor electrodes the interplay between capacitance and charge transport is poorly understood. In our view, the biggest difficulty is the lack of real understanding of the factors influencing the transport of charge from redox site to external circuit *via* the nanoconductor material. Other problems are associated with the composite production technique which is generally cumbersome or costly and not suitable for real commercial devices.[50,51] One manifestation of this is the fact that impressive data associated with very thin electrodes are often presented without the corresponding data for the thick electrodes that are required by industry. This is an issue because, as described above, for low-conductivity electrodes severe degradation of performance with increased thickness is to be expected.

In this work we address these problems. Using MnO_2 nanoplatelets as a model 2D system, we demonstrate a simple method to produce supercapacitor electrodes based on solution processing. We show that the capacitance of these electrodes falls off with increasing electrode thickness and scan rate as would be expected for a material limited by low electrical conductivity. Equally problematic, the electrodes are not mechanically robust and become unstable beyond thicknesses of 1.7 μm. To resolve these issues, we use simple solution-processing techniques to prepare composite electrodes of MnO_2 nanoplatelets mixed with carbon nanotubes. We show that the electrical conductivity of such composites can be tuned over 8 orders of magnitude and is controlled by percolation theory. Electrochemical testing is used to demonstrate that the addition of even small amounts of nanotubes has a dramatic effect on charge storage properties, with up to $\times$25 increase in capacitance observed at scan rates of $\sim$1000 mV/s. Importantly, we explore the mechanism, finding the capacitance increase to scale with nanotube volume fraction as predicted by percolation theory. Another practical advantage of this approach is that the composite electrodes were much more mechanically robust, allowing the production of much thicker films giving up to a 40-fold increase in areal capacitance compared to MnO_2 alone.

RESULTS AND DISCUSSION

Single Component Films of MnO_2 or Single-Walled Nanotubes (SWNT). Layered manganese dioxide was prepared by a modified version[52] of the coprecipitation method described by Jiang *et al.*[45] (see Methods). This procedure results in a brown dispersion containing ~0.2 mg/mL MnO_2 dispersed in isopropanol. TEM analysis (Figure 1A,B) showed the dispersed material to be in the form of thin nanoplatelets with mean lateral size of ~200 nm (see Supporting Information Figure S1). We note that such samples always contain a small population of relatively large crumpled objects such as the one at the bottom of Figure 1B. Thin films of MnO_2 nanoplatelets were produced by vacuum filtration for Raman and XPS analysis. A typical Raman spectrum is shown in Figure 1C and displays a dominant feature at ~645 cm^{-1}, which we attribute to the symmetric stretching vibration ν_2(Mn−O) of MnO_6, as expected for layered MnO_2.[53−55] The shoulder observed on the left-hand side of this primary peak (~575 cm^{-1}) can be attributed to the ν_3(Mn−O) stretching vibration associated with MnO_6 octahedra.[56] XPS measurements of the Mn 2p and O 1s core-levels (Figure 1D,E) show the expected MnO_2 components in the correct stoichiometry, with a ratio of manganese to oxygen very close to 50%. The Mn 2p3/2 peak has been fitted with five multiplet components in accordance with the parameters established for MnO_2 by Biesinger *et al.*[57] The additional Mn^{3+} component can be attributed to X-ray damage and/or other oxide species like Mn_2O_3, but only constitutes a very minor part of the spectrum. Apart from the main MnO_2 component, the deconvoluted O 1s peak also shows contributions from the SiO_2 substrate, nitrates which are most likely associated with the $Mn(NO_3)_2$ starting material and a minor contribution from adventitious carbonates. This analysis clearly shows the synthesized material to be predominately layered MnO_2.

Once the nature of the dispersed material was confirmed, we used vacuum filtration to prepare a range of thin films with varying nanoplatelet mass per unit area (*M*/*A*). The mass was controlled *via* the volume of dispersion filtered while a small quantity (10 wt %) of ethyl cellulose (EC) was added as a binder. The film *M*/*A* varied from 2 to 160 $\mu g/cm^2$, a relatively broad range as compared to previous work (Comparison: Pang *et al.*,[37] 1−14 $\mu g/cm^2$; Hu *et al.*,[58] 130−150 $\mu g/cm^2$). After filtration, pieces of the films ($A \sim 0.25$ cm^2) were transferred from the nitrocellulose filter membranes onto ITO-coated glass current collectors, using acetone to dissolve the membrane.[59]

Film thicknesses were determined using profilometry, revealing that the *M*/*A* loading range corresponds to thickness varying from 40 nm to 1.7 μm (see Supporting Information Figure S2). Despite the inclusion of the ethyl cellulose, we found it impossible to prepare electrodes of the MnO_2 thicker than 1.7 μm, due to poor mechanical properties leading to difficulties in transfer. We measured the film density as 0.95 g/cm^3 suggesting a high film porosity of ~80% (using ρ_{MnO_2} = 5 g/cm^3). This morphology is attractive for electrochemical capacitor applications due to the combination of high of surface to bulk atomic ratio and porosity, enabling ready access of electrolyte counterions to internal surface area of the electrode.

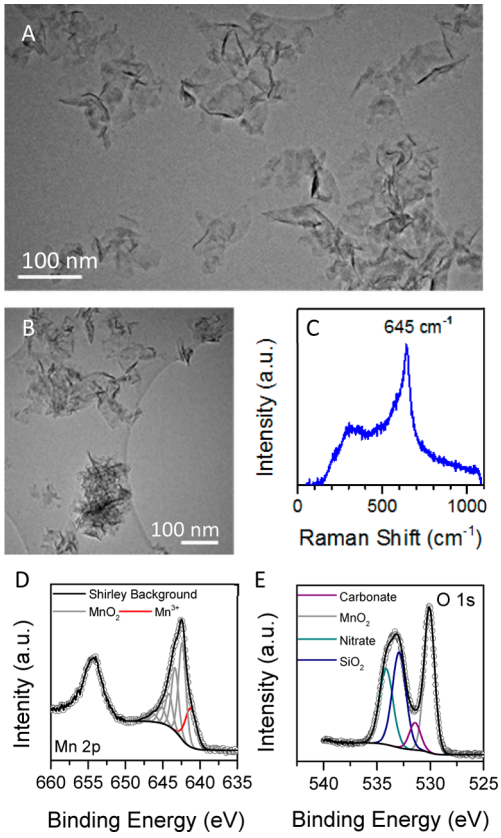

Figure 1. Characterization of MnO_2 nanoplatelets. (A and B) TEM images of MnO_2 nanoplatelets. (C) Raman spectrum measured on vacuum-filtered thin film of MnO_2 nanoplatelets. (D and E) XPS spectrum measured on vacuum filtered thin film of MnO_2 nanoplatelets showing (D) Mn 2p peaks and (E) O 1s peaks.

Electrochemical testing was performed to investigate the charge storage properties of the MnO_2 films. Cyclic voltammetry (CV) was carried out using 0.5 M K_2SO_4 electrolyte in a three electrode configuration. Before measurement, each film was conditioned by applying 50 CV cycles between 0.1 and 0.8 V *versus* Ag/AgCl (dV/dt = 100 mV/s) to ensure a stable electrochemical response. Next, CVs were recorded at a variety of scan rates from 10 to 5000 mV/s. The slowest and fastest scan rates correspond to charging/discharging times of 70 and 0.14 s, respectively. These charging/discharging times are suitable for many supercapacitor applications.[60]

The typical CV response of an ultrathin MnO_2 electrode ($t \sim 40$ nm) at two scan rates (50 and 5000 mV/s) is shown in Figure 2A. To facilitate comparison, we

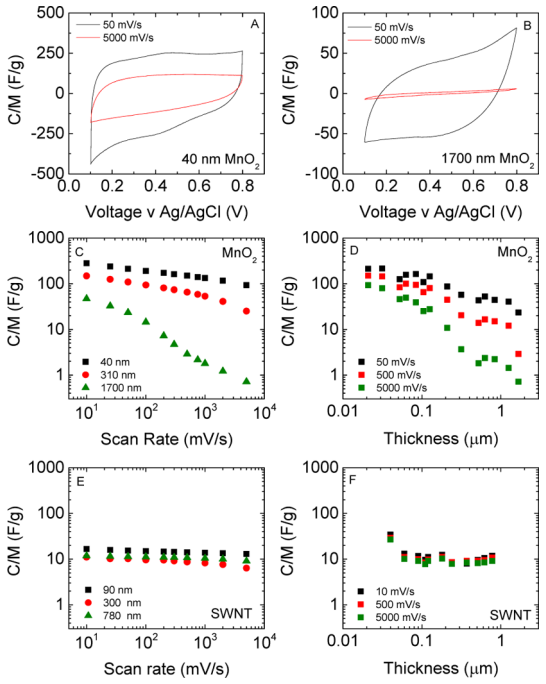

Figure 2. Characterization of MnO_2 thin film supercapacitor electrodes. (A and B) Cyclic voltammograms, measured at two scan rates for electrodes prepared from MnO_2 films with thickness of (A) 40 nm and (B) 1700 nm. (C) Specific capacitance for MnO_2 films of three different thicknesses plotted *versus* scan rate. (D) Specific capacitance of MnO_2 films measured at three different scan rates, plotted *versus* film thickness. (E) Specific capacitance of SWNT films for three different thicknesses plotted *versus* scan rate. (F) Specific capacitance of SWNT films measured at three different scan rates plotted *versus* film thickness.

normalized the current response to both scan rate and the mass of active material, yielding a differential gravimetric capacitance. The shape of the CV curves are broad and near-rectangular, typical of the pseudocapacitive response of this material[44] at 50 mV/s; Faradaic features can be discerned, centered at 0.5 V on oxidation, and 0.4 V on reduction. A slow current rise, even for the thin film electrodes, indicated the presence of resistive character. The capacitance was calculated by integrating the current passed within the potential window (see Methods). We calculated a relatively high specific capacitance (*C/M*) for this material (~200 F/g at 50 mV/s), typical for a thin film of MnO_2 charged relatively slowly.[58,61] This value decreases only slightly at very high scan rate (~90 F/g at 5000 mV/s).

Characterization of films with thickness in the nanometer range is useful to evaluate the quality of the material. However, for many applications where greater absolute capacitance is required, the electrode thickness needs to be scaled up. Therefore, it is important to evaluate how capacitance varies with electrode thickness. To investigate this we have prepared thicker electrodes and evaluated their charge storage behavior in a similar manner. Figure 2B shows a CV of a 1.7 μm thick MnO_2 film. We observe that C/M has decreased by a factor of ~10 at 50 mV/s and a factor of ~100 at 5000 mV/s, compared with the 40 nm film. The CV shape exhibits a more resistor-like behavior for thicker films, and the Faradaic features observed for the thin films are no longer perceivable, even at low scan rates (Supporting Information Figure S4). We emphasize that even these MnO_2 films are still relatively thin; commercial supercapacitor electrodes based on porous carbon typically have thicknesses of 10−100s of microns.[62]

To demonstrate this behavior more clearly we have plotted C/M as a function of scan rate for three different electrode thicknesses (Figure 2C) and as a function of thickness for three different scan rates (Figure 2D). In both cases, we observe impaired specific capacitance when going to thicker films and faster charge/discharge rates. As described in the introduction, such results are consistent with electrodes which are limited by poor electrical performance.[22,33,37,39,48,63−68] In particular, the symmetry between these temporal and spatial dependencies suggests they are determined by the same underlying electrode properties, namely those determining the transport of charge between active sites and the external circuit. Using the four-probe technique, we measured the electrical conductivity of the thin films of MnO_2 nanoplatelets used here to be $\sim 1.7 \times 10^{-5}$ S/m. This low conductivity is similar to values reported by others[40,41] and would be expected to limit supercapacitor performance. Understanding how these effects can be overcome is crucial for the design of supercapacitor electrodes with high absolute capacitance, particularly at high power.

In contrast, the high electrical conductivity of many carbon-based materials (among other reasons) makes them excellent candidates as high performance supercapacitor electrodes. To compare with the MnO_2 data described above, we have prepared disordered network films of single walled carbon nanotubes (SWNTs) of various thicknesses. We measured the film conductivity to be $\sim 2 \times 10^5$ S/m, which is in agreement with previous reports.[69] Cyclic voltammetry, carried out under the same conditions as for MnO_2, showed highly rectangular behavior (see Supporting Information Figure S3), indicating close to an ideal capacitive response with a small time constant. The gravimetric capacitance was virtually invariant with both thickness and scan rate at ~10 F/g (Figure 2E,F), as reported by other authors.[49,70]

It is clear from this work that thin films of MnO_2 have great potential as supercapacitor electrodes but are limited by the poor conductivity resulting in disappointing performance at high rates and electrode thickness. Indeed, overcoming electronic transport limitations of pseudocapacitive materials in general is key to achieving high performance electrodes. As discussed by a number of authors,[49,63] a simple solution is to add carbon nanotubes to the MnO_2 electrode resulting in the formation of a conducting network to

facilitate transport of charge from redox sites to the external circuit. Furthermore, this strategy is known to improve mechanical properties of films containing layered materials and may assist with electrolyte accessibility by preventing restacking of adjacent sheets.[27,71]

Composite Films of MnO_2 and SWNT. To test the effect of adding carbon nanotubes to films of MnO_2 nanoplatelets, we prepared composite films with a range of SWNT/MnO_2 mass ratios. This was achieved by simple mixing of appropriate volumes of the two component dispersions followed by vacuum filtration and film transfer (see Methods). In this study, we chose a fixed loading of MnO_2 (160 μg/cm^2) to which increasing quantities of SWNTs were added, forming composites with nanotube mass fractions of up to 40 wt % ($M_f = M_{NT}/(M_{NT} + M_{MnO2})$). This method of composition variation differs somewhat from others[72,73] where the total film mass is kept constant and the masses of both components are altered simultaneously. By keeping the MnO_2 mass constant for all films, our approach makes analysis of the way MnO_2 pseudocapacitance varies with film composition more straightforward. In doing so, we found that while the film thickness is relatively constant at ~1.5 μm up to M_f = 20 wt %, addition of SNWTs beyond this loading caused the film thickness to increase, reaching ~3 μm for a mass fraction ~40 wt % (see Supporting Information Figure S5). The fixed MnO_2 *M/A* of 160 μg/cm^2 was chosen because it corresponds to the greatest thickness at which we could produce mechanically robust MnO_2-only films for comparison, and is a thickness where the capacitance of MnO_2 is clearly electrically limited (Figure 2C,D). Additionally, while it remained relatively thin, we minimized the influence of ionic transport which cannot be ignored for very thick electrodes.

SEM images of an MnO_2-only film and two composite films (M_f = 1 and 25 wt %) are shown in Figure 3A–C. Even at 1 wt % loading, the presence of the nanotubes is apparent. The images at higher loadings suggest effective mixing of the two components, with the MnO_2 intimately incorporated within the nanotube network. One very important point is that addition of any amount of SWNTs greatly improved the film's mechanical integrity, making the inclusion of binder (EC) unnecessary. This is not unexpected as we have previously observed films of exfoliated 2D materials to be very brittle, but to become much more robust on addition of nanotubes.[6,74] This contrasts with previously reported composite electrodes where the conductive additive has not also acted as binder.[44,75] In addition, the composite films are extremely porous, containing free volumes of >75% for all mass fractions (see Supporting Information, Figure S5). This is advantageous as it should allow free access of the electrolyte to the internal surface of the electrode. On the other hand, a high porosity will ultimately reduce the scope for high volumetric capacitance.

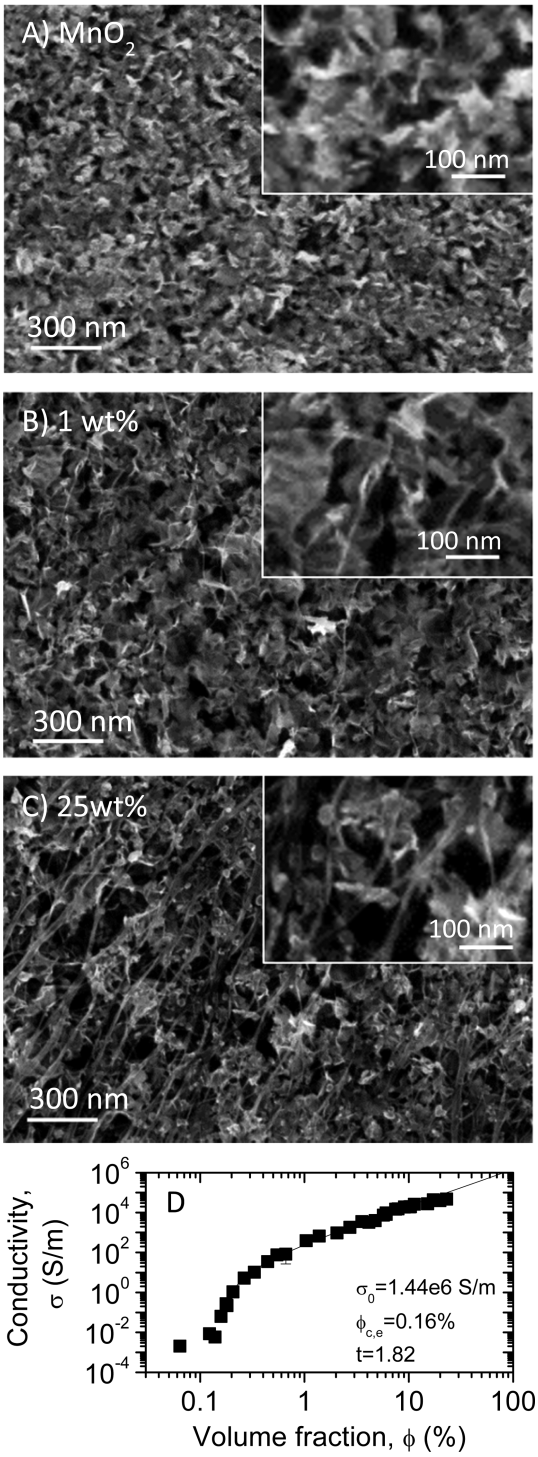

Figure 3. SWNT/MnO_2 composite thin films. (A–C) SEM images of (A) a thin MnO_2 film, (B) a composite film with 1 wt % SWNTs and (C) a composite film with 25 wt % SWNTs. In (A–C), the film thicknesses were ~100 nm while the insets show magnified regions. (D) In-plane electrical conductivity of thin films plotted *versus* SWNT volume fraction. The line is a fit to percolation theory eq 1 with the fit constants given in the panel. In all cases, the films in D were 1.5–3 μm thick.

Using the four-probe technique, we measured the in-plane electrical conductivity for MnO_2/SWNT

composites with a range of nanotube contents. The conductivity data is plotted in Figure 3D where the nanotube content is represented as the volume fraction, ϕ ($\phi = V_{NT}/(V_{NT} + V_{MnO2})$). We found that the DC conductivity increases rapidly with addition of small amounts of nanotubes, reaching ~100 S/m for ϕ = 1 vol % and approaching 10^5 S/m for $\phi = 25$ vol %. This behavior is qualitatively similar to that observed previously for composites of MoS_2 nanoplatelets mixed with carbon nanotubes.[6,47] The electrical properties of such insulator/nanoconductor composites is described by percolation theory.[76] In this framework, the film conductivity is expected to be very low until a critical volume fraction of nanoconductors is reached, the electrical percolation threshold, $\phi_{c,e}$. Above the percolation threshold, the conductivity is described by[76]

$$\sigma = \sigma_0(\phi - \phi_{c,e})^n \quad (1)$$

where σ_0 is related to the conductivity of the nanoconductor and n is the percolation exponent.[77] Fitting our data gives a very low electrical percolation threshold of $\phi_{c,e}$ = 0.16 vol %, σ_0 of 1.4 × 10^6 S/m and a percolation exponent of 1.82. We note that the percolation threshold for composites with 1D fillers is thought to scale with the diameter to length ratio of the filler particles.[78] Thus, very low percolation thresholds such as that found here are often observed for composites based on carbon nanotubes.[77] This is a significant advantage for our purpose, as a small percolation threshold means significant conductivities can be achieved at relatively low ϕ, meaning very little capacitive material has to be sacrificed to introduce the conductive paths.

Composite Supercapacitor Electrodes. If relatively thick MnO_2-only electrodes display capacitances which are limited by the electrical conductivity of MnO_2, the data in Figure 3D would lead us to expect the addition of nanotubes to result in significant capacitance enhancements. To test this, we measured CVs for a range of composites as well as single component films. In all cases, the MnO_2 mass was kept constant at 160 μg/cm^2 resulting in film thicknesses in the range 1.5−3 μm (Supporting Information Figure S5). Shown in Figure 4A are the current responses of three composite films to linear potential sweeps with dV/dt = 1000 mV/s. The first thing to note is a considerable increase in current density as nanotube content is increased. This strongly supports the idea that the introduction of conductive paths facilitates charge transport to redox sites. However, the shape of the CV curves is also of interest. The response of a simple series resistor-capacitor model is given by

$$j = \frac{C}{A}\frac{dV}{dt}(1 - e^{-t/\tau}) \quad (2)$$

where j is the current density, A is the device area, and $\tau = R_{ESR}C$ (R_{ESR} is the equivalent series resistance which

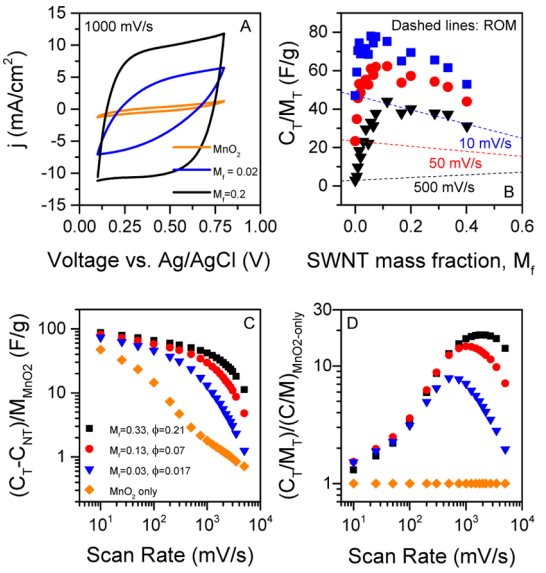

Figure 4. Initial characterization of MnO_2/SWNT composite thin films as supercapacitor electrodes. (A) Cyclic voltammograms for electrodes prepared from MnO_2 and MnO_2/SWNT composites with SWNT mass fractions of 2 and 20 wt %. (B) Measured total capacitance, C_T, divided by total electrode mass, M_T, measured for composite electrodes plotted *versus* SWNT mass fraction, M_f, for three scan rates, 10, 50, and 500 mV/s (color coded with dashed lines). The dashed lines represent the specific capacitance calculated from the Rule of Mixtures (ROM) as would be expected if MnO_2 and SWNT were contributing to the capacitance with no additional effects occurring. (C) Specific capacitance associated only with MnO_2 (*i.e.*, with SWNT contribution removed) measured for composite electrodes plotted *versus* scan rates for a number of SWNT mass fractions. In the caption, the SWNT volume fraction, ϕ, is also given. (D) Increase in specific capacitance due to the presence of SWNTs relative to MnO_2-only electrodes plotted *versus* scan rate for a number of SWNT mass fractions (see panel C for key). In all cases, the films in D were 1.5−2 μm thick.

is closely related to the electrode resistance[79]). It is clear that increasing the SWNT content results in reduced τ, suggesting a substantial reduction of R_{ESR} due to the presence of the nanotubes. This effect is also evident, though less pronounced, at slow scan rates (Supporting Information Figure S4) and even with 33 wt % nanotubes, the subtle Faradiac features of the MnO_2-only films can be discerned. Similar observations regarding CV shape were made by Lee *et al.*[39] and Kim *et al.*[48] on adding carbon black to MnO_2.

We can quantify this capacitance increase by plotting the measured capacitance of the composite film, C_T, normalized to total film mass, M_T, measured at three scan rates, as a function of nanotube mass fraction in Figure 4B (N.B. $M_T = M_{MnO2} + M_{NT}$ and assuming both MnO_2 and NTs contribute to the capacitance, $C_T = C_{MnO2} + C_{NT}$). It is clear that, for all scan rates, the capacitance increases dramatically upon addition of even a few percent of nanotubes before falling off at high mass fraction. The SWNT loading providing maximum capacitance falls in the range of 5−15 wt %, shifting slightly to higher loadings with increasing scan rate. In some cases, the improvements are

impressive: for the 500 mV/s data, a ×15 increase in C_T/M_T was observed at M_f = 11 wt % compared to the MnO_2-only electrode. Beyond the optimized values, the specific capacitance decreases as the relative nanotube content in the films increases, approaching the nanotube-only value of ~10 F/g (a value which was invariant with scan rate over the range studied in this work). Overall, this behavior is not what would be expected from the rule of mixtures (dashed lines), as would apply if both MnO_2 and SWNTs were contributing to the capacitance only as per their individual specific capacitances.

The peaked behavior observed in Figure 4B has been observed before in supercapacitors formed from mixtures of activated carbon/carbon black[80] and carbon aerogels filled with nanoconductors such as carbon black, nanotubes and carbon fibers.[81] In both of these publications, it was suggested that the peak capacitance occurred at the percolation threshold. However, comparing the results in Figure 3D and Figure 4B shows the peak capacitance to occur at volume fractions substantially above the electrical percolation threshold. This optimum loading of carbon nanotubes (5−15 wt %) is relatively low compared to the literature where (often unoptimized and therefore poorly justified) conductor contents tend to fall in the range 15−25%.[39,44,48,49,70,82−85] Obviously lower conductor contents are desirable from an economic standpoint given the present relative cost of these two materials.

That the capacitance data in Figure 4B does not follow the rule of mixtures suggests the increase in capacitance is due to the addition of conducting paths to the MnO_2 electrode. The presence of these paths seemingly "activates" the nearby MnO_2 by enabling the transport of stored charge to and from the current collector. To examine this suggestion, we should consider the effect of nanotube content on the specific capacitance due only to the MnO_2. To do this, we subtract off the contribution to the capacitance associated with the nanotubes (*i.e.*, estimated using C_{NT}/M_{NT} of 10 F/g) and normalize to the mass of MnO_2 (*i.e.*, we calculate $(C_T - C_{NT})/M_{MnO2}$). This data is shown in Figure 4C plotted *versus* scan rate for composite electrodes with a number of nanotube contents. Shown for comparison is the equivalent data for an MnO_2-only film of equivalent M/A. This data shows the presence of nanotubes to considerably increase the capacitance associated with the MnO_2 at all scan rates. However, the effect is particularly apparent at high scan rates with the MnO_2 capacitance increasing from ~2 F/g in the MnO_2-only film to ~42 F/g for the film with 33 wt % SWNT (dV/dt = 1000 mV/s). That these increases are due to conductivity enhancement rather than morphological effects in response to the addition of nanotubes can be seen by measuring the film porosity as a function of nanotube content (see Supporting Information Figure S5B). This data clearly shows the porosity to be invariant with nanotube content ruling out the possibility that the nanotubes somehow open the network, allowing easier access of ions to the internal surface.

In practical terms, what is important is the increase in specific electrode capacitance which can be achieved by adding nanotubes. To show this, we plot the ratio of the specific capacitance of a composite electrode to that for an MnO_2-only electrode (*i.e.*, $(C_T/M_T)/(C/M)_{MnO2\text{-only}}$) *versus* scan rate in Figure 4D for a number of mass fractions. While a ×2 increase is found at low scan rates, much larger increases are found at higher scan rates. The relative capacitance increase peaks at scan rates of ~600−2000 mV/s with a ×20 increase observed at 2000 mV/s for the 33 wt % sample.

Percolation of Capacitance in Composite Films. To allow future optimization of solution-processed nanostructured supercapacitor electrodes, it will be necessary to understand the nature of these capacitance increases. The increase in MnO_2 capacitance compared to an MnO_2-only electrode, normalized by MnO_2 mass, is given by

$$(\Delta C/M)_{MnO2} = \frac{C_T - C_{NT} - C_{MnO2\text{-only}}}{M_{MnO2}} \quad (3)$$

We note that calculation of this parameter is facilitated by the fact that all films have identical MnO_2 mass as described above and in Methods. Shown in Figure 5A is $(\Delta C/M)_{MnO2}$ plotted *versus* nanotube volume fraction, ϕ, for data collected at two representative scan rates. As illustrated by these plots, data collected at all scan rates display the same features: at low ϕ, $(\Delta C/M)_{MnO2}$ increases nonlinearly with ϕ up to $\phi = \phi_{sat}$, after which it reaches a constant value which we denote $(\Delta C/M)_{sat}$. We will first discuss the low ϕ behavior before turning to the saturation regime.

As discussed above, it is likely that the observed increases in capacitance are associated with the introduction of conducting paths to the electrode. The conductivity of the overall network is controlled by percolation theory (Figure 3D). However, it has previously been shown that, for supercapacitor electrodes based on percolating nanotube networks, the resulting capacitance is also described by percolation theory.[79] This occurs because the capacitance is directly proportional to the number of nanotubes connected to the network, a parameter which is controlled by percolation theory.[76,79] It is likely that similar phenomena are present in the MnO_2/SWNT composites under study here. We propose that, as the nanotube volume fraction increases and the network becomes more extensive, the volume of MnO_2 within close proximity of the network increases. This proximate MnO_2 can easily transfer charge to the current collector *via* the nanotube network and so becomes "activated". Thus, we expect the capacitance to scale with network size and

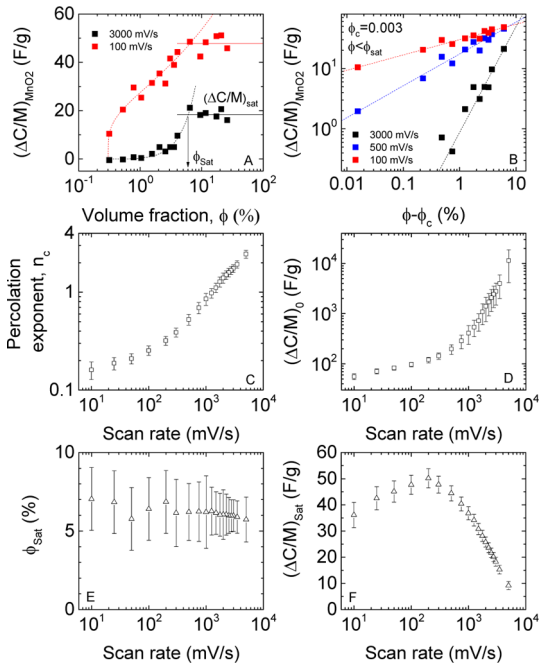

Figure 5. Percolation analysis of thin film supercapacitor electrodes. (A) Increase in specific capacitance of MnO_2 due to percolative effect $(\Delta C/M)_{MnO2} = (C_T - C_{NT} - C_{MnO2\text{-}only})/M_{MnO2}$ (*i.e.*, with SWNT contribution and capacitance of equivalent MnO_2-only film subtracted off), measured at two different scan rates, plotted *versus* SWNT volume fraction. In all cases, the capacitance saturated at a value of $(\Delta C/M)_{Sat}$ (solid line) for volume fractions above a critical value, ϕ_{sat}. The dashed lines are fits to percolation theory eq 3. (B) Percolation scaling graphs for specific capacitance increase. In all cases, the percolation threshold was ϕ_c = 0.3 vol %. The lines represent fits to percolation theory eq 3. Only data with $\phi < \phi_{sat}$ is shown. (C and D) Percolation fit parameters plotted *versus* scan rate: the percolation exponent, n_c (C) and $(\Delta C/M)_0$ (D). (E and F) Saturated volume fraction, ϕ_{sat} (E) and saturation capacitance $(\Delta C/M)_{Sat}$ (F) both plotted *versus* scan rate.

propose that the capacitance increase to be described by a percolative scaling law of the form:

$$(\Delta C/M)_{MnO2} = (\Delta C/M)_0(\phi - \phi_{c,c})^{n_c} \qquad (4)$$

where $(\Delta C/M)_0$ is a constant, $\phi_{c,c}$ is the capacitive percolation threshold and n_c is the capacitive percolation exponent. We note that, in general, the $(\Delta C/M)_{MnO_2}$ *versus* ϕ data is quite scattered, making it difficult to accurately fit a three-unknown function such as eq 4 to the data. To address this, we fixed $\phi_{c,c}$ at a constant value for all scan rates. Initial trials found that setting $\phi_{c,c} = \phi_{c,e} = 0.0016$ gave reasonable fits for all scan rates. However, it was found that using $\phi_{c,c}$ = 0.003 gave clearly better fits, especially at low ϕ (15 out of 19 scan rates displayed $R^2 > 0.9$). This can be seen by plotting $(\Delta C/M)_{MnO_2}$ *versus* $\phi - \phi_C$ as shown in Figure 5B. This justifies our proposal to use eq 4 and suggests the capacitance is indeed described by percolation theory.

The fact that $\phi_{c,c} > \phi_{c,e}$ is perhaps not unexpected. The electrical measurements were associated with current flowing in the plane of the composite. However, in the capacitance measurements the composite electrode sits on top of an ITO current collector, with the electrolyte in contact with the top composite surface. In this case, current flow from ITO to redox sites is, on average, out of plane. In thin film composites, we expect the nanotubes to be randomly arranged in the plane of the film but partially aligned with the film surface making in−plane and out-of-plane charge transport nonequivalent. In fact, it has been shown that the percolation threshold for aligned rods is higher than that for randomly arranged rods[86] making the difference between $\phi_{c,c}$ and $\phi_{c,e}$ unsurprising.

Fitting gave $(\Delta C/M)_0$ and n_c with reasonably low uncertainties for a range of scan rates between 10 and 5000 mV/s. These data are shown in Figure 5C,D. The capacitive percolation exponent increases monotonically with scan rate from $n_c \sim 0.2$ for dV/dt = 10 mV/s to $n_c \sim 3$ for dV/dt = 5000 mV/s. This is somewhat unexpected as for electrical percolation, the percolation exponent tends to be a property of the network, depending on parameters such as network uniformity[87] or width of the junction resistance distribution.[88] Such network properties would not be expected to vary with scan rate. The scan rate dependence of $(\Delta C/M)_0$ is also poorly understood. It follows a similar form as the n_c *versus* rate data, increasing continuously with rate. By analogy with electrical percolation,[78] we would expect $(\Delta C/M)_0$ to reflect the material properties of the system. As with the capacitive percolation exponent, we would not expect such a material property to vary with scan rate. However, we suggest that to some extent these variations in the fit parameters with scan rate may reflect an influence of ionic diffusion constraints, which become important at higher rates. Thorough examination of these effects will require knowledge of how ionic diffusion properties within the electrode vary with nanotube loading in these composites, which is an important question for future work. However, what is not in doubt is that the relative capacitance increase associated with MnO_2 is consistent with percolation theory.

It is probably easier to understand the saturated behavior. As ϕ is increased, the network becomes more extensive, bringing more and more MnO_2 within proximity of nanotubes. However, at some critical volume fraction, ϕ_{sat}, all MnO_2 in the electrode will be close enough to a nanotube to effectively exchange charge with the network. After this, the capacitance cannot be increased by increasing the volume fraction and it saturates at a value of $(\Delta C/M)_{sat}$. The saturation volume fraction, ϕ_{sat}, is plotted *versus* scan rate in Figure 5E and clearly is constant at ~6 vol %. This invariance implies that the maximum distance (R) over which MnO_2 can exchange charge with the network is scan rate independent. This maximum range defines a shell, of thickness R, which surrounds the nanotube network and defines the volume of activated MnO_2, *i.e.*, the MnO_2 which can effectively transfer charge to

the nanotube network. The saturation volume fraction is then the lowest volume fraction where the shell encloses all the MnO_2 in the electrode. Considering a local section of shell, associated with a straight section of nanotube (radius r), both of which we model as cylinders, the saturation volume fraction is approximately the nanotube volume divided by the volume enclosed by the shell: $\phi_{sat} = r^2/(r + R)^2$. Taking ϕ_{sat} = 6 vol % gives $R \approx 3r$. Assuming that the nanotubes are in the form of bundles of diameter ~20 nm (as observed previously[69]), means that $r \sim 10$ nm, giving $R \sim 30$ nm.

The dependence of $(\Delta C/M)_{sat}$ on scan rate is shown in Figure 5F. Interestingly, $(\Delta C/M)_{sat}$ increases at low scan rate before reaching a maximum at ~200 mV/s. We note that the position of this maximum is controlled by the details of the rate dependence of both n_c and $(\Delta C/M)_0$. However, it is the presence of this maximum that results in the shape of the curves given in Figure 4D.

This work clearly demonstrates the importance of percolation in composite supercapacitors. While a number of papers have suggested percolation to play a role in the operation of composite supercapacitors,[80,81,89] even indicating the onset of capacitance at the electrical percolation threshold,[30] percolation scaling of capacitance has not been observed. We note that Pico *et al.*, when studying nanotube/activated carbon composite, observed rule of mixtures rather than percolative behavior.[89] However, it is likely that this due to the relatively high conductivity of the capacitive phase and the moderate difference in conductivities between the components of the composite (×1000 compared with > $\times 10^8$ here). We believe the current study is the first demonstration of percolation of capacitance in composite supercapacitor electrodes (although percolation scaling of capacitance has been observed in single-component nanotube networks).[79] Understanding the nature of such percolation will be critical for the optimization of capacitive composites.

Thick Composite Films. As described in the introduction, working supercapacitors must display large areal capacitances, C/A, to maximize their energy storage capacity. Because $C/A = \rho t C_T/M_T$, where ρ and t are electrode density and thickness, respectively, maximization of areal capacitance requires C_T/M_T to remain high even as the film thickness is maximized. However, as described above, electrodes of MnO_2 nanoplatelets display two significant problems. First, like all resistive electrode materials C_T/M_T tends to fall with increasing thickness. Second, and equally serious is the problem of poor mechanical integrity of MnO_2 electrodes. As described above, we found it impossible to prepare MnO_2-only electrodes with $t > 1.7$ μm due to severe brittleness. We expect both of these problems to be addressed by the production of MnO_2–nanotube composites. To test this, we produced a set of composite electrodes (ϕ = 15 vol %, well in the saturated regime)

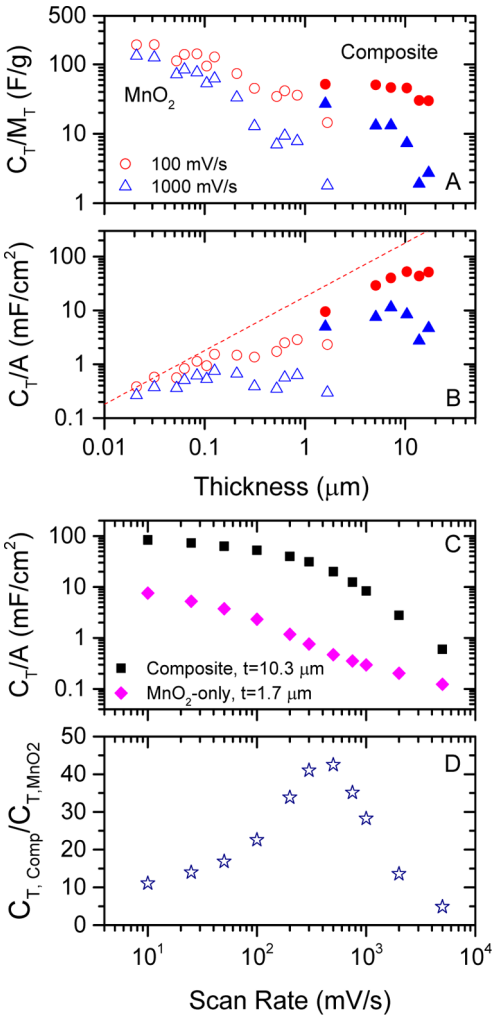

Figure 6. (A) Specific capacitance and (B) areal capacitance as a function of electrode thickness. This data is shown for electrodes produced from both MnO_2-only (open symbols) and MnO_2–SWNT composite (15 vol %, closed symbols) films, measured at two different scan rates. (C) Areal capacitance plotted *versus* scan rate for the thickest MnO_2-only electrode we were able to produce and a 15 vol % SWNT–MnO_2 composite electrode with optimized thickness. (D) Ratio of the capacitance of composite and MnO_2-only electrodes shown in (C) plotted *versus* scan rate. This data shows the increase in capacitance achievable by adding nanotubes due to the combination of percolative effects and the ability to make thicker electrodes in the presence of nanotubes.

with thicknesses between 1.6 and 17 μm. In all cases the electrodes were mechanically robust with no problems associated with brittleness.

We performed CV measurements to measure the capacitance of these electrodes for a number of scan rates. Shown in Figure 6A is the specific capacitance, C_T/M_T, measured at two scan rates, plotted as a function of thickness (solid symbols). For comparison, the equivalent data is also shown for MnO_2-only electrodes (open symbols). While the MnO_2-only capacitance tends to fall off with increasing thickness, it is clear that the composites have higher capacitance for a given thickness compared to the MnO_2-only.

In addition, for the 100 mV/s data, the measured values of C_T/M_T remain roughly constant as thickness is increased. For the 1000 mV/s data, C_T/M_T falls with increasing thickness, probably because at this high rate the capacitance becomes diffusion limited. However, even at 1000 mV/s, the capacitance is much higher in the composite than would be achieved for thicker MnO_2-only films *if they could be made*.

Probably more useful is to plot the data as C_T/A as we have done in Figure 6B. Here, the MnO_2-only data increases sublinearly (linearity indicated by dashed line) with t. However, for the composite, the 100 mV/s data increases linearly, reaching 52 mF/cm^2 at t = 10.3 μm. In addition, even though the 1000 mV/s composite data increases sublinearly, the best composite still displays 11.4 mF/cm^2, considerably larger than the best MnO_2 film. Similar values were obtained by Okamura *et al.*[90] who prepared Mn/Mo mixed oxide composite electrodes with carbon nanotubes, measuring 20.4 mF/cm^2 for a 4.1 μm film (100 mV/s in 0.5 M Na_2SO_4 electrolyte) and Wen *et al.*[91] who prepared MnO_2 composites with carbon black, measuring 20 mF/cm^2 for a 20 μm film (10 mV/s, 0.1 M KCl).

In Figure 6C, we compare the areal capacitance for the thickest MnO_2-only film (t = 1.7 μm) with that of the best performing composite film (t = 10.3 μm). It is clear that the composite massively outperforms the MnO_2-only film at all scan rates. We can quantify the improvement shown in Figure 6C by plotting the ratio of composite to MnO_2-only capacitances *versus* scan rate in Figure 6D. This graph shows a better than 10-fold improvement in areal capacitance at all scan rates below ~3000 mV/s. Indeed at scan rates close to 500 mV/s, enhancements of ×40 are achieved. We note that these improvements are due to the combination of improved MnO_2 capacitance due to improved electrical transport and the ability to prepare thicker electrodes due to the presence of nanotubes.

CONCLUSIONS

We have demonstrated that supercapacitor electrodes can be easily fabricated by solution processing methods from MnO_2 nanoplatelets and MnO_2–nanotube composites. The MnO_2-only electrodes displayed capacitances which fell off rapidly with increasing charge/discharge rate and electrode thickness. This is consistent with observations by other authors and is due to the poor electrical conductivity of the MnO_2. However, on addition of nanotubes, we found the electrode conductivity to increase by 8 orders of magnitude in a manner described by percolation theory. Because of the increased conductivity, we observed large increases in capacitance, especially at high rates where a >10-fold increase in specific capacitance was observed. This capacitance increase is due to the nanotube network facilitating charge transport from redox sites to the external circuit. We found that the increase in specific capacitance associated with MnO_2 alone increased with nanotube volume fraction as described by percolation theory. However, the percolation fit parameters varied with scan rate in a manner that is currently not understood. At high nanotube content, the specific capacitance associated with MnO_2 alone saturated. The saturation volume fraction was ~6 vol %, a value we associate with the nanotube network activating the entire MnO_2 volume. We test the applicability of these results by preparing thick binder-free MnO_2-nanotube composites. We find the areal capacitance to be up to 40 times higher than the best MnO_2-only electrode we could prepare.

To translate the excellent intrinsic charge storage properties of 2D materials into real applications requires they be processed into films and other macroscopic structures. However, for these to be useful the problem of poor electrical conductivity must also be addressed. Here we show that when adding a chosen nanoconductor to form composite films, percolation theory applies not only to the way electrical properties vary with composition but also the extent to which interfacial processes can occur throughout the film as a result of the created electrical pathways. We believe these insights pertain not only to the design of nanostructured supercapacitor electrodes, but to any electrochemical application requiring charge transport between interfacial sites and the external circuit through a nanostructured network current collector.

METHODS

Preparation of MnO_2 Dispersions. Manganese dioxide powder was prepared as described by Jiang *et al.*[45] In brief, 1.7 g of $Mn(NO_3)_2$ and 0.5 g of poly(ethylene glycol)–poly(propylene glycol)–poly(ethylene glycol) triblock copolymer (P123) were dissolved into 100 mL of distilled water. The solution was heated to 45 °C and 100 mL of 0.1 M $KMnO_4$(aq) was added dropwise under vigorous stirring. The obtained precipitate was filtered under pressure, washed with distilled water, and allowed to dry for 24 h. Chemicals were supplied by Sigma-Aldrich, 99.99% purity.

The resulting MnO_2 powder was then exfoliated by bath sonication to form a stable dispersion in isopropyl alcohol (MnO_2 starting concentration, 10 mg/mL). Sonication was carried out for 3 h using a FisherBrand 11207 sonic bath (37 kHz, 200 W). The dispersion was then centrifuged for 30 min at 1500 rpm using a Heraeus Multifuge X1 Centrifuge to remove any unstable material.

A stock solution of ethyl cellulose (EC, Sigma-Aldrich) was prepared by dissolving this polymer in isopropyl alcohol (IPA) while heating at 75 °C (EC concentration, 5 mg/mL). This solution was then added to the stock MnO_2 solution, such that the EC binder/MnO_2 ratio was 1:10. Ethyl cellulose was used as a binder for neat MnO_2 films to improve mechanical integrity.

Preparation of Carbon Nanotube Dispersions. A stock solution of sodium dodecyl sulfate (SDS, Sigma-Aldrich) was prepared by adding this surfactant to Millipore water to an SDS concentration of 5 mg/mL. This solution was then added to arc-discharge single-walled carbon nanotube powder (SWNTs, Iljin Nanotech Co.)

such that the surfactant/SWNT mass ratio in the resultant dispersions was 5:1 (SWNT concentration, 1 mg/mL). Each dispersion received 5 min of high power tip sonication (VibraCell CVX; 750W, 20% 60 kHz), was then placed in a sonic bath (Branson 1510-MT sonic bath, 20 kHz) for 1 h, followed by another 5 min of tip sonication. The dispersions were then centrifuged at 5500 rpm for 90 min. The supernatant of each dispersion was carefully decanted and combined for further use. We obtained the concentration after centrifugation by measuring the absorbance spectrum (Varian Cary 6000i spectrophotometer) and recording the absorbance per unit length, A/l. Using the Lambert–Beer law, the final concentration was calculated using the known extinction coefficient of the SWNT (3389 mL/(mg/m) at 660 nm).

Film Preparation. MnO_2 and SWNT only films, and composites of both these materials, were prepared by first diluting the stock MnO_2/EC dispersion 10-fold with Millipore water and then combining it with the required amount of the stock SWNT dispersion. All films were prepared by vacuum filtration of the diluted dispersion using porous mixed cellulose ester filter membranes (MF-Millipore membrane, hydrophilic, 0.025 μm pore size, 47 mm diameter). The resulting films (diameter, 36 mm) were cut to the desired dimensions and transferred to polyethylene terephthalate (PET), indium tin oxide (ITO), and Au-coated silicon substrates for electrical conductivity testing, electrochemical testing, and SEM imaging, respectively. The cellulose filter membrane was removed by treatment with acetone vapor and subsequent acetone liquid baths.

Film Characterization. Film thickness was measured by profilometry using a Dektak 6M, Veeco Instruments. Step profiles were obtained at three locations on the film and averaged. Electrical conductivity values were calculated from resistivity measurements made using a four-point probe technique with a Keithley 2400 source meter (Keithley Instruments, Inc.) and LabView interface (National Instruments, Inc.). Agar Scientific supplied silver paint electrodes were attached to the films and the film width (~4 mm) and electrode separations (~10 mm) were carefully recorded. SEM was performed using a ZEISS Ultra Plus (Carl Zeiss Group). During imaging the accelerating voltage was 5 kV, with a 30 μm aperture and a working distance of approximately 5 mm.

X-ray photoelectron spectroscopy was performed under ultrahigh vacuum conditions (<5.10−10 mbar), using monochromated Al Kα X-rays (1486.6 eV) from an Omicron XM1000 MkII X-ray source and an Omicron EA125 energy analyzer. An Omicron CN10 electron flood gun was used for charge compensation and the binding energy scale was referenced to the C 1s core-level of the adventitious carbon at 285 eV. The O 1s and Mn 2p core-levels were recorded at an analyzer pass energy of 20 eV and with slit widths of 6 mm (entry) and 3 mm × 10 mm (exit). After subtraction of a Shirley background, the spectra were fitted with Gaussian–Lorentzian line shapes.

Raman analysis was performed using a Witec Alpha 300 R with a 532 nm excitation wavelength and an 1800 lines/mm grating. Average spectra were obtained for each sample from line scans consisting of 50 discrete spectra, each with an integration time of 5 min, taken over a line 200 μm in length. A laser power of 400 μW, as measured using a LaserCheck power meter, was employed to minimize sample damage.

Electrochemical properties of the films were examined using cyclic voltammetry in a three electrode electrochemical cell. The cell consisted of a Ag/AgCl reference electrode and an amorphous carbon counter electrode with 0.5 M K_2SO_4 electrolyte. Electrodes were first cycled at 100 mV/s for 50 cycles between 0.1 and 0.8 V to ensure stable charge/discharge behavior, followed by 20 cycles each at various scan rates from 10 to 5000 mV/s (corresponding to charge/discharge times from 0.14 to 70 s). Film capacitance was estimated from the cyclic voltammograms by integrating the current passed during the positive and negative potential sweeps:

$$\frac{C}{M} = \frac{1}{(M/A)\Delta V(\mathrm{d}V/\mathrm{d}t)} \int_{v}^{v+\Delta v} j \, \mathrm{d}V$$

where M/A is mass per unit area, j is areal current density, ΔV is potential window (0.7 V), and $\mathrm{d}V/\mathrm{d}t$ is scan rate. This calculation provides the gravimetric capacitance over the entire potential window and we average the positive and negative portions of the curve. Film area was typically 0.25 cm^2.

Conflict of Interest: The authors declare no competing financial interest.

Acknowledgment. We thank Science Foundation Ireland (11/PI/1087) and the European Research Council (SEMANTICS) for financial support. We acknowledge the CRANN Advanced Microscopy Lab for technical support. N.B. and G.S.D. acknowledge SFI under PI_10/IN.1/I3030. N.M.C. acknowledges the EU under FP7-2010-PPP Electrograph (No. 266391). V.N. thanks both ERC (2DNanocaps) and SFI for support.

Supporting Information Available: Flake size histogram for MnO_2, film thickness as a function of loading for MnO_2 films; CVs for a SWNT only electrode; CVs for MnO_2 and selected composites at 50 mV/s; thickness and porosity as a function of loading for composite films. This material is available free of charge *via* the Internet at http://pubs.acs.org.

REFERENCES AND NOTES

1. Geim, A. K. Graphene: Status and Prospects. *Science* **2009**, *324*, 1530–1534.
2. Chhowalla, M.; Shin, H. S.; Eda, G.; Li, L.-J.; Loh, K. P.; Zhang, H. The Chemistry of Two-Dimensional Layered Transition Metal Dichalcogenide Nanosheets. *Nat. Chem.* **2013**, *5*, 263–275.
3. Wang, Q. H.; Kalantar-Zadeh, K.; Kis, A.; Coleman, J. N.; Strano, M. S. Electronics and Optoelectronics of Two-Dimensional Transition Metal Dichalcogenides. *Nat. Nanotechnol.* **2012**, *7*, 699–712.
4. Osada, M.; Sasaki, T. Two-Dimensional Dielectric Nanosheets: Novel Nanoelectronics from Nanocrystal Building Blocks. *Adv. Mater.* **2012**, *24*, 210–228.
5. Liu, H.; Neal, A. T.; Zhu, Z.; Luo, Z.; Xu, X.; Tománek, D.; Ye, P. D. Phosphorene: An Unexplored 2D Semiconductor with a High Hole Mobility. *ACS Nano* **2014**, *8*, 4033–4041.
6. Coleman, J. N.; Lotya, M.; O'Neill, A.; Bergin, S. D.; King, P. J.; Khan, U.; Young, K.; Gaucher, A.; De, S.; Smith, R. J.; *et al.* Two-Dimensional Nanosheets Produced by Liquid Exfoliation of Layered Materials. *Science* **2011**, *331*, 568–571.
7. Nicolosi, V.; Chhowalla, M.; Kanatzidis, M. G.; Strano, M. S.; Coleman, J. N. Liquid Exfoliation of Layered Materials. *Science* **2013**, *340*, 1420.
8. Zeng, Z. Y.; Yin, Z. Y.; Huang, X.; Li, H.; He, Q. Y.; Lu, G.; Boey, F.; Zhang, H. Single-Layer Semiconducting Nanosheets: High-Yield Preparation and Device Fabrication. *Angew. Chem. Int. Ed.* **2011**, *50*, 11093–11097.
9. Eda, G.; Yamaguchi, H.; Voiry, D.; Fujita, T.; Chen, M.; Chhowalla, M. Photoluminescence from Chemically Exfoliated MoS_2. *Nano Lett.* **2011**, *11*, 5111–5116.
10. Lukatskaya, M. R.; Mashtalir, O.; Ren, C. E.; Dall'Agnese, Y.; Rozier, P.; Taberna, P. L.; Naguib, M.; Simon, P.; Barsoum, M. W.; Gogotsi, Y. Cation Intercalation and High Volumetric Capacitance of Two-Dimensional Titanium Carbide. *Science* **2013**, *341*, 1502–1505.
11. Liu, J.; Liu, X.-W. Two-Dimensional Nanoarchitectures for Lithium Storage. *Adv. Mater.* **2012**, *24*, 4097–4111.
12. Backes, C.; Smith, R. J.; McEvoy, N.; Berner, N. C.; McCloskey, D.; Nerl, H. C.; O'Neill, A.; King, P. J.; Higgins, T.; Hanlon, D.; *et al.* Edge and Confinement Effects Allow *in Situ* Measurement of Size and Thickness of Liquid-Exfoliated Nanosheets. *Nat. Commun.* **2014**, *5*, 4576.
13. Voiry, D.; Yamaguchi, H.; Li, J.; Silva, R.; Alves, D. C. B.; Fujita, T.; Chen, M.; Asefa, T.; Shenoy, V. B.; Eda, G.; *et al.* Enhanced Catalytic Activity in Strained Chemically Exfoliated WS2 Nanosheets for Hydrogen Evolution. *Nat. Mater.* **2013**, *12*, 850–855.
14. Wang, J.-Z.; Lu, L.; Lotya, M.; Coleman, J. N.; Chou, S.-L.; Liu, H.-K.; Minett, A. I.; Chen, J. Development of MoS_2-Cnt Composite Thin Film from Layered MoS_2 for Lithium Batteries. *Adv. Energy Mater.* **2013**, *3*, 798–805.

15. Chang, K.; Chen, W. L-Cysteine-Assisted Synthesis of Layered Mos2/Graphene Composites with Excellent Electrochemical Performances for Lithium Ion Batteries. *ACS Nano* **2011**, *5*, 4720–4728.
16. Tai, S.-Y.; Liu, C.-J.; Chou, S.-W.; Chien, F. S.-S.; Lin, J.-Y.; Lin, T.-W. Few-Layer MoS_2 Nanosheets Coated onto Multi-Walled Carbon Nanotubes as a Low-Cost and Highly Electrocatalytic Counter Electrode for Dye-Sensitized Solar Cells. *J. Mater. Chem.* **2012**, *22*, 24753–24759.
17. Suzuki, S.; Miyayama, M. Lithium Intercalation Properties of Octatitanate Synthesized through Exfoliation/Reassembly. *J. Phys. Chem. B* **2006**, *110*, 4731–4734.
18. Wang, L. Z.; Takada, K.; Kajiyama, A.; Onoda, M.; Michiue, Y.; Zhang, L. Q.; Watanabe, M.; Sasaki, T. Synthesis of a Li-Mn-Oxide with Disordered Layer Stacking through Flocculation of Exfoliated MnO_2 Nanosheets, and Its Electrochemical Properties. *Chem. Mater.* **2003**, *15*, 4508–4514.
19. Lee, C. Y.; Tsai, H. M.; Chuang, H. J.; Li, S. Y.; Lin, P.; Tseng, T. Y. Characteristics and Electrochemical Performance of Supercapacitors with Manganese Oxide-Carbon Nanotube Nanocomposite Electrodes. *J. Electrochem. Soc.* **2005**, *152*, A716–A720.
20. Park, H.-Y.; Shin, T. J.; Joh, H.-I.; Jang, J. H.; Ahn, D.; Yoo, S. J. Graphene-Oxide-Intercalated Layered Manganese Oxides as an Efficient Oxygen Reduction Reaction Catalyst in Alkaline Media. *Electrochem. Commun.* **2014**, *41*, 35–38.
21. Son, J. S.; Choi, M. K.; Han, M. K.; Park, K.; Kim, J. Y.; Lim, S. J.; Oh, M.; Kuk, Y.; Park, C.; Kim, S. J.; *et al.* N-Type Nanostructured Thermoelectric Materials Prepared from Chemically Synthesized Ultrathin Bi_2Te_3 Nanoplates. *Nano Lett.* **2012**, *12*, 640–647.
22. Conway, B. E. *Electrochemical Supercapacitors: Scientific Fundamentals and Technological Applications*, 1 ed.; Springer: Boston, MA, 1999.
23. Sugimoto, W.; Iwata, H.; Yasunaga, Y.; Murakami, Y.; Takasu, Y. Preparation of Ruthenic Acid Nanosheets and Utilization of Its Interlayer Surface for Electrochemical Energy Storage. *Angew. Chem., Int. Ed.* **2003**, *42*, 4092–4096.
24. Brezesinski, T.; Wang, J.; Tolbert, S. H.; Dunn, B. Ordered Mesoporous α-MoO_3 with Iso-Oriented Nanocrystalline Walls for Thin-Film Pseudocapacitors. *Nat. Mater.* **2010**, *9*, 146–151.
25. Toupin, M.; Brousse, T.; Belanger, D. Charge Storage Mechanism of MnO_2 Electrode Used in Aqueous Electrochemical Capacitor. *Chem. Mater.* **2004**, *16*, 3184–3190.
26. Yu, W.; Jiang, X.; Ding, S.; Li, B. Q. Preparation and Electrochemical Characteristics of Porous Hollow Spheres of NiO Nanosheets as Electrodes of Supercapacitors. *J. Power Sources* **2014**, *256*, 440–448.
27. Wang, G.; Huang, J.; Chen, S.; Gao, Y.; Cao, D. Preparation and Supercapacitance of CuO Nanosheet Arrays Grown on Nickel Foam. *J. Power Sources* **2011**, *196*, 5756–5760.
28. Sugimoto, W.; Yokoshima, K.; Ohuchi, K.; Murakami, Y.; Takasu, Y. Fabrication of Thin-Film, Flexible, and Transparent Electrodes Composed of Ruthenic Acid Nanosheets by Electrophoretic Deposition and Application to Electrochemical Capacitors. *J. Electrochem. Soc.* **2006**, *153*, A255–A260.
29. Rakhi, R. B.; Chen, W.; Hedhili, M. N.; Cha, D.; Alshareef, H. N. Enhanced Rate Performance of Mesoporous Co_3O_4 Nanosheet Supercapacitor Electrodes by Hydrous Ruo2 Nanoparticle Decoration. *ACS Appl. Mater. Interfaces* **2014**, *6*, 4196–4206.
30. Hanlon, D.; Backes, C.; Higgins, T. M.; Hughes, M.; O'Neill, A.; King, P. J.; McEvoy, N.; Duesberg, G. S.; Mendoza Sanchez, B.; Pettersson, H.; *et al.* Production of Molybdenum Trioxide Nanosheets by Liquid Exfoliation and Their Application in High-Performance Supercapacitors. *Chem. Mater.* **2014**, *26*, 1751–1763.
31. Sun, X.; Wang, G.; Hwang, J.-Y.; Lian, J. Porous Nickel Oxide Nano-Sheets for High Performance Pseudocapacitance Materials. *J. Mater. Chem.* **2011**, *21*, 16581.
32. Song, M.-S.; Lee, K. M.; Lee, Y. R.; Kim, I. Y.; Kim, T. W.; Gunjakar, J. L.; Hwang, S.-J. Porously Assembled 2D Nanosheets of Alkali Metal Manganese Oxides with Highly Reversible Pseudocapacitance Behaviors. *J. Phys. Chem. C* **2010**, *114*, 22134–22140.
33. Wang, L.; Lin, C.; Zhang, F.; Jin, J. Phase Transformation Guided Single-Layer B-$Co(OH)_2$ Nanosheets for Pseudocapacitive Electrodes. *ACS Nano* **2014**, *8*, 3724–3734.
34. Zhu, J.; Cao, L.; Wu, Y.; Gong, Y.; Liu, Z.; Hoster, H. E.; Zhang, Y.; Zhang, S.; Yang, S.; Yan, Q.; *et al.* Building 3D Structures of Vanadium Pentoxide Nanosheets and Application as Electrodes in Supercapacitors. *Nano Lett.* **2013**, *13*, 5408–5413.
35. Ma, R.; Liu, X.; Liang, J.; Bando, Y.; Sasaki, T. Molecular-Scale Heteroassembly of Redoxable Hydroxide Nanosheets and Conductive Graphene into Superlattice Composites for High-Performance Supercapacitors. *Adv. Mater.* **2014**, *26*, 4173–4178.
36. Paton, K. R.; Varrla, E.; Backes, C.; Smith, R. J.; Khan, U.; O'Neill, A.; Boland, C.; Lotya, M.; Istrate, O. M.; King, P. J.; *et al.* Scalable Production of Large Quantities of Defect-Free Few-Layer Graphene by Shear Exfoliation in Liquids. *Nat. Mater.* **2014**, *13*, 624–630.
37. Pang, S.-C.; Anderson, M. A.; Chapman, T. W. Novel Electrode Materials for Thin-Film Ultracapacitors: Comparison of Electrochemical Properties of Sol-Gel-Derived and Electrodeposited Manganese Dioxide. *J. Electrochem. Soc.* **2000**, *147*, 444–450.
38. Broughton, J. N.; Brett, M. J. Investigation of Thin Sputtered Mn Films for Electrochemical Capacitors. *Electrochim. Acta* **2004**, *49*, 4439–4446.
39. Lee, H. Y.; Kim, S. W.; Lee, H. Y. Expansion of Active Site Area and Improvement of Kinetic Reversibility in Electrochemical Pseudocapacitor Electrode. *Electrochem. Solid-State Lett.* **2001**, *4*, A19–A22.
40. Belanger, D.; Brousse, T.; Long, J. W. Manganese Oxides: Battery Materials Make the Leap to Electrochemical Capacitors. *Electrochem. Soc. Interface* **2008**, *17*, 49–52.
41. Xu, C.; Kang, F.; Li, B.; Du, H. Recent Progress on Manganese Dioxide Based Supercapacitors. *J. Mater. Res.* **2010**, *25*, 1421–1432.
42. Raymundo-Pinero, E.; Khomenko, V.; Frackowiak, E.; Beguin, F. Performance of Manganese Oxide/Cnts Composites as Electrode Materials for Electrochemical Capacitors. *J. Electrochem. Soc.* **2005**, *152*, A229–A235.
43. Yu, G.; Hu, L.; Liu, N.; Wang, H.; Vosgueritchian, M.; Yang, Y.; Cui, Y.; Bao, Z. Enhancing the Supercapacitor Performance of Graphene/MnO_2 Nanostructured Electrodes by Conductive Wrapping. *Nano Lett.* **2011**, *11*, 4438.
44. Lee, H. Y.; Goodenough, J. B. Supercapacitor Behavior with KCl Electrolyte. *J. Solid State Chem.* **1999**, *144*, 220–223.
45. Jiang, H.; Sun, T.; Li, C.; Ma, J. Hierarchical Porous Nanostructures Assembled from Ultrathin MnO_2 Nanoflakes with Enhanced Supercapacitive Performances. *J. Mater. Chem.* **2011**, *22*, 2751–2756.
46. Zhi, M.; Xiang, C.; Li, J.; Li, M.; Wu, N. Nanostructured Carbon–Metal Oxide Composite Electrodes for Supercapacitors: A Review. *Nanoscale* **2012**, *5*, 72–88.
47. Cunningham, G.; Lotya, M.; McEvoy, N.; Duesberg, G. S.; van der Schoot, P.; Coleman, J. N. Percolation Scaling in Composites of Exfoliated MoS_2 Filled with Nanotubes and Graphene. *Nanoscale* **2012**, *4*, 6260–6264.
48. Kim, H.; Popov, B. N. Synthesis and Characterization of MnO_2-Based Mixed Oxides as Supercapacitors. *J. Electrochem. Soc.* **2003**, *150*, D56–D62.
49. Zhou, Y. K.; He, B. L.; Zhang, F. B.; Li, H. L. Hydrous Manganese Oxide/Carbon Nanotube Composite Electrodes for Electrochemical Capacitors. *J. Solid State Electrochem* **2004**, *8*, 482–487.
50. Hu, C.-C.; Tsou, T.-W. Capacitive and Textural Characteristics of Hydrous Manganese Oxide Prepared by Anodic Deposition. *Electrochim. Acta* **2002**, *47*, 3523–3532.
51. Wei, W.; Cui, X.; Chen, W.; Ivey, D. G. Phase-Controlled Synthesis of MnO_2 Nanocrystals by Anodic Electrodeposition: Implications for High-Rate Capability Electrochemical Supercapacitors. *J. Phys. Chem. C* **2008**, *112*, 15075–15083.
52. Coelho, J.; Mendoza-Sanchez, B.; Pettersson, H.; Pokle, A.; McGuire, E. K.; Long, E.; McKeon, L.; Bell, A. P.; Nicolosi, V., Manganese Oxide Nanosheets and a 2D Hybrid of Graphene-Manganese Oxide Nanosheets Synthesized by

Liquid-Phase Exfoliation. 2014, arXiv:1409.1087 [cond-mat.mtrl-sci]. arXiv.org e-Print archive. http://arxiv.org/abs/1409.1087.
53. Julien, C.; Massot, M.; Baddour-Hadjean, R.; Franger, S.; Bach, S.; Pereira-Ramos, J. P. Raman Spectra of Birnessite Manganese Dioxides. *Solid State Ionics* **2003**, *159*, 345–356.
54. Hsu, Y.-K.; Chen, Y.-C.; Lin, Y.-G.; Chen, L.-C.; Chen, K.-H. Birnessite-Type Manganese Oxides Nanosheets with Hole Acceptor Assisted Photoelectrochemical Activity in Response to Visible Light. *J. Mater. Chem.* **2012**, *22*, 2733–2739.
55. Hsu, Y.-K.; Chen, Y.-C.; Lin, Y.-G.; Chen, L.-C.; Chen, K.-H. Reversible Phase Transformation of MnO_2 Nanosheets in an Electrochemical Capacitor Investigated by *in Situ* Raman Spectroscopy. *Chem. Commun.* **2011**, *47*, 1252–1254.
56. Ogata, A.; Komaba, S.; Baddour-Hadjean, R.; Pereira-Ramos, J. P.; Kumagai, N. Doping Effects on Structure and Electrode Performance of K-Birnessite-Type Manganese Dioxides for Rechargeable Lithium Battery. *Electrochim. Acta* **2008**, *53*, 3084–3093.
57. Biesinger, M. C.; Payne, B. P.; Grosvenor, A. P.; Lau, L. W. M.; Gerson, A. R.; Smart, R. S. Resolving Surface Chemical States in Xps Analysis of First Row Transition Metals, Oxides and Hydroxides: Cr, Mn, Fe, Co and Ni. *Appl. Surf. Sci.* **2011**, *257*, 2717–2730.
58. Hu, C.-C.; Tsou, T.-W. Ideal Capacitive Behavior of Hydrous Manganese Oxide Prepared by Anodic Deposition. *Electrochem. Commun.* **2002**, *4*, 105–109.
59. Wu, Z. C.; Chen, Z. H.; Du, X.; Logan, J. M.; Sippel, J.; Nikolou, M.; Kamaras, K.; Reynolds, J. R.; Tanner, D. B.; Hebard, A. F.; *et al.* Transparent, Conductive Carbon Nanotube Films. *Science* **2004**, *305*, 1273–1276.
60. Miller, J. R. Introduction to Electrochemical Capacitor Technology. *IEEE Electr. Insul. Mag.* **2010**, *26*, 40–47.
61. Zhu, G.; Li, H.; Deng, L.; Liu, Z.-H. Low-Temperature Synthesis of Δ-MnO_2 with Large Surface Area and Its Capacitance. *Mater. Lett.* **2010**, *64*, 1763–1765.
62. Stoller, M. D.; Ruoff, R. S. Best Practice Methods for Determining an Electrode Material's Performance for Ultracapacitors. *Energy Environ. Sci.* **2010**, *3*, 1294.
63. Wu, Y.-T.; Hu, C.-C. Effects of Electrochemical Activation and Multiwall Carbon Nanotubes on the Capacitive Characteristics of Thick MnO_2 Deposits. *J. Electrochem. Soc.* **2004**, *151*, A2060–A2066.
64. Chen, Y.-S.; Hu, C.-C.; Wu, Y.-T. Capacitive and Textural Characteristics of Manganese Oxide Prepared by Anodic Deposition: Effects of Manganese Precursors and Oxide Thickness. *J. Solid State Electrochem.* **2004**, *8*, 467–473.
65. Broughton, J. N.; Brett, M. J. Variations in MnO_2 Electrodeposition for Electrochemical Capacitors. *Electrochim. Acta* **2005**, *50*, 4814–4819.
66. Nam, K.-W.; Kim, K.-B. Manganese Oxide Film Electrodes Prepared by Electrostatic Spray Deposition for Electrochemical Capacitors. *J. Electrochem. Soc.* **2006**, *153*, A81–A88.
67. Nagarajan, N.; Cheong, M.; Zhitomirsky, I. Electrochemical Capacitance of Mnox Films. *Mater. Chem. Phys.* **2007**, *103*, 47–53.
68. Wimalasiri, Y.; Fan, R.; Zhao, X. S.; Zou, L. Assembly of Ni-Al Layered Double Hydroxide and Graphene Electrodes for Supercapacitors. *Electrochim. Acta* **2014**, *134*, 127–135.
69. Doherty, E. M.; De, S.; Lyons, P. E.; Shmeliov, A.; Nirmalraj, P. N.; Scardaci, V.; Joimel, J.; Blau, W. J.; Boland, J. J.; Coleman, J. N. The Spatial Uniformity and Electromechanical Stability of Transparent, Conductive Films of Single Walled Nanotubes. *Carbon* **2009**, *47*, 2466–2473.
70. Subramanian, V.; Zhu, H.; Wei, B. Synthesis and Electrochemical Characterizations of Amorphous Manganese Oxide and Single Walled Carbon Nanotube Composites as Supercapacitor Electrode Materials. *Electrochem. Commun.* **2006**, *8*, 827–832.
71. Lu, X.; Dou, H.; Gao, B.; Yuan, C.; Yang, S.; Hao, L.; Shen, L.; Zhang, X. A Flexible Graphene/Multiwalled Carbon Nanotube Film as a High Performance Electrode Material for Supercapacitors. *Electrochim. Acta* **2011**, *56*, 5115–5121.
72. Toupin, M.; Brousse, T.; Belanger, D. Influence of Microstucture on the Charge Storage Properties of Chemically Synthesized Manganese Dioxide. *Chem. Mater.* **2002**, *14*, 3946–3952.
73. Lee, S. W.; Kim, J.; Chen, S.; Hammond, P. T.; Shao-Horn, Y. Carbon Nanotube/Manganese Oxide Ultrathin Film Electrodes for Electrochemical Capacitors. *ACS Nano* **2010**, *4*, 3889–3896.
74. Khan, U.; O'Connor, I.; Gun'ko, Y. K.; Coleman, J. N. The Preparation of Hybrid Films of Carbon Nanotubes and Nano-Graphite/Graphene with Excellent Mechanical and Electrical Properties. *Carbon* **2010**, *48*, 2825–2830.
75. Brousse, T.; Toupin, M.; Belanger, D. A Hybrid Activated Carbon-Manganese Dioxide Capacitor Using a Mild Aqueous Electrolyte. *J. Electrochem. Soc.* **2004**, *151*, A614–A622.
76. Stauffer, D. S.; Aharony, A. *Introduction to Percolation Teory*; Taylor and Francis: London, 1994.
77. Bauhofer, W.; Kovacs, J. Z. A Review and Analysis of Electrical Percolation in Carbon Nanotube Polymer Composites. *Compos. Sci. Technol.* **2009**, *69*, 1486–1498.
78. Foygel, M.; Morris, R. D.; Anez, D.; French, S.; Sobolev, V. L. Theoretical and Computational Studies of Carbon Nanotube Composites and Suspensions: Electrical and Thermal Conductivity. *Phys. Rev. B* **2005**, *71*, 104201.
79. King, P. J.; Higgins, T. M.; De, S.; Nicoloso, N.; Coleman, J. N. Percolation Effects in Supercapacitors with Thin, Transparent Carbon Nanotube Electrodes. *ACS Nano* **2012**, *6*, 1731–1741.
80. Wu, N. L.; Wang, S. Y. Conductivity Percolation in Carbon–Carbon Supercapacitor Electrodes. *J. Power Sources* **2002**, *110*, 233–236.
81. Lv, G.; Wu, D.; Fu, R.; Zhang, Z.; Su, Z. Electrochemical Properties of Conductive Filler/Carbon Aerogel Composites as Electrodes of Supercapacitors. *J. Non-Cryst. Solids* **2008**, *354*, 4567–4571.
82. Yang, X.-h.; Wang, Y.-g.; Xiong, H.-m.; Xia, Y.-y. Interfacial Synthesis of Porous Mno2 and Its Application in Electrochemical Capacitor. *Electrochim. Acta* **2007**, *53*, 752–757.
83. Yuan, A.; Wang, X.; Wang, Y.; Hu, J. Textural and Capacitive Caracteristics of Mno2 Nnocrystals Derived from a Novel Slide-Reaction Route. *Electrochim. Acta* **2009**, *54*, 1021–1026.
84. Reddy, R. N.; Reddy, R. G. Sol-Gel MnO_2 as an Electrode Material for Electrochemical Capacitors. *J. Power Sources* **2003**, *124*, 330–337.
85. Wang, G.-X.; Zhang, B.-L.; Yu, Z.-L.; Qu, M.-Z. Manganese Oxide/Mwnts Composite Electrodes for Supercapacitors. *Solid State Ionics* **2005**, *176*, 1169–1174.
86. White, S. I.; DiDonna, B. A.; Mu, M.; Lubensky, T. C.; Winey, K. I. Simulations and Electrical Conductivity of Percolated Networks of Finite Rods with Various Degrees of Axial Alignment. *Phys. Rev. B* **2009**, *79*, 024301.
87. Scardaci, V.; Coull, R.; Lyons, P. E.; Rickard, D.; Coleman, J. N. Spray Deposition of Highly Transparent, Low-Resistance Networks of Silver Nanowires over Large Areas. *Small* **2011**, *7*, 2621–2628.
88. Balberg, I. Tunnelling and Nonuniversal Conductivity in Composite-Materials. *Phys. Rev. Lett.* **1987**, *59*, 1305–1308.
89. Pico, F.; Pecharroman, C.; Ansón, A.; Martínez, M. T.; Rojo, J. M. Understanding Carbon–Carbon Composites as Electrodes of Supercapacitors a Study by Ac and Dc Measurements. *J. Electrochem. Soc.* **2007**, *154*, A579–A586.
90. Okamura, K.; Inoue, R.; Sebille, T.; Tomono, K.; Nakayama, M. An Approach to Optimize the Composition of Supercapacitor Electrodes Consisting of Manganese-Molybdenum Mixed Oxide and Carbon Nanotubes. *J. Electrochem. Soc.* **2011**, *158*, A711.
91. Wen, S.; Lee, J.-W.; Yeo, I.-H.; Park, J.; Mho, S.-i. The Role of Cations of the Electrolyte for the Pseudocapacitive Behavior of Metal Oxide Electrodes, MnO_2 and RuO_2. *Electrochim. Acta* **2004**, *50*, 849–855.